Journal of
Materials Chemistry C
Materials for optical, magnetic and electronic devices

Accepted Manuscript

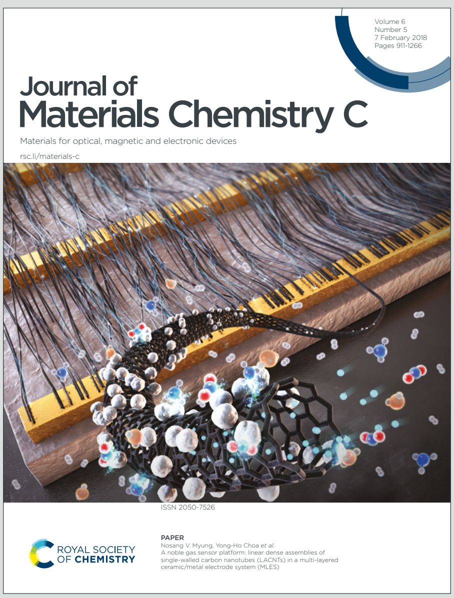

View Article Online
DOI: 10.1039/D5TC01126D

Mapping the Polymorphic Phase Transformations of $CsPbI_3$ Perovskite Thin Films

Rudolph Holley III,[1] Quinn C. Burlingame,[1,*] and Yueh-Lin Loo[1,*]

[1] Department of Chemical and Biological Engineering, Princeton University, Princeton, New Jersey, United States

* Correspondence: qb@princeton.edu and lloo@princeton.edu

Abstract

Inorganic perovskite $CsPbI_3$ has a bandgap of 1.7 eV, making it an ideal complementary absorber to Si for integration into tandem solar cells. However, the black, photoactive $CsPbI_3$ phases are metastable and readily transform into a yellow non-perovskite δ-$CsPbI_3$ phase at room temperature, posing a significant challenge to long-term device stability. In this study, we investigate the temperature-dependent dynamics of these phase transitions in $CsPbI_3$ thin films using a combination of *in situ* X-ray diffraction and time-resolved optical microscopy. We find the transformation rate to be highly temperature-dependent, with the fastest conversion occurring at 225°C, where 50% of the film transformed to δ-$CsPbI_3$ within 17 minutes. To identify processing temperatures with longer phase-stability windows, we used the time- and temperature-dependent phase dynamics data to generate a time-temperature-transformation diagram for thin film $CsPbI_3$. Processing near the peak conversion temperature must be completed within two minutes to retain black-phase purity, while processing above 280°C or below 150°C provides a much wider processing window with <1% conversion to δ-$CsPbI_3$ occurring after 10 minutes. Conversely, it may be useful to hold $CsPbI_3$ solar cells or thin films with phase-stabilizing modifications near 225°C to accelerate potential phase transitions and maximally stress their stability.

Introduction

Lead-halide perovskite solar cells (PSCs) have emerged as a promising energy harvesting technology in recent years due to their rapidly increasing solar-to-electric power conversion efficiencies,[1–5] and the tunable optoelectronic properties and low-cost energy-efficient processability of perovskites.[1–3] Of particular interest are tandem photovoltaics comprising perovskite top cells with lower bandgap bottom cells, such as Si. Tandems reduce thermalization losses of high-energy photons by absorbing them in a wide bandgap top cell, while transmitting low-energy photons to the bottom cell, resulting in combined efficiencies higher than either sub-cell can achieve alone. An ideal top cell to pair with Si in a tandem cell requires an absorber with a bandgap of approximately 1.7 eV, which can be achieved with hybrid organic-inorganic perovskite alloys and inorganic $CsPbI_3$.[6–9] Among these options, $CsPbI_3$ is a

View Article Online
DOI: 10.1039/D5TC01126D

particularly promising candidate for such applications because it lacks volatile organic cations that can lead to thermochemical instability in hybrid PSCs.[7–11] However, $CsPbI_3$ is polymorphic as shown in **Fig. S1,** and its most thermodynamically stable phase at room temperature is its yellow non-perovskite orthorhombic phase (δ-$CsPbI_3$) with poor optoelectronic properties. The cubic polymorph (α-$CsPbI_3$) is only stable at high temperatures (>320°C),[12,13] while the other black photoactive phases of $CsPbI_3$ (tetragonal β-$CsPbI_3$ and orthorhombic γ-$CsPbI_3$) are only metastable at room temperature.[11] Thus, even with active layers kinetically trapped in these phases, they will spontaneously convert to δ-$CsPbI_3$ given time, leading to catastrophic PSC performance degradation.

To address this challenge, considerable research effort has been devoted to understanding the phase behavior of $CsPbI_3$ and to stabilizing β- and γ-$CsPbI_3$ at room temperature.[14–18] Calculations from Zhao et al. suggest that γ-$CsPbI_3$ can be stabilized by reducing the size of $CsPbI_3$ grains to ~100 nm, which sufficiently increases their surface area-to-bulk ratio.[19] Our group has since integrated this nanocrystalline morphology into highly stable PSCs with projected lifetimes >50,000 hours of continuous operation, though this lifetime came at the expense of reduced power-conversion efficiency compared to PSCs comprising large-grain $CsPbI_3$ active layers.[20–22] It has also been observed that the interfacial strain between $CsPbI_3$ and underlying transport layers has a significant role in governing phase transition rates.[16,17,23–25] For example, Liu et al. reported that β-$CsPbI_3$ films could be phase stabilized by depositing a thin organic layer between the perovskite and the underlying electron transport layer.[25] Previous studies have also mapped the equilibrium phase transitions of $CsPbI_3$ powders (including solid-state synthesis routes and decomposition pathways at elevated temperatures in the presence of oxygen)—for instance, prior work on $CsPbI_3$ powders revealed rapid synthesis at 400°C but eventual decomposition into Cs_4PbI_6 over longer timescales,[12] while thermal degradation studies in air highlighted instability above 350–400°C due to oxidation and phase segregation.[26]

In this study, we detail the time- and temperature-dependent kinetics of $CsPbI_3$ phase transitions in a device-relevant thin-film form factor without any phase-stabilizing interventions. We measured the temperature-dependent dynamics of the black $CsPbI_3$ phases as they transform into δ-$CsPbI_3$ with *in situ* x-ray diffraction (XRD), and we used time-resolved optical microscopy to measure the propagation velocity of δ-$CsPbI_3$ grain boundaries as the films transform. Unlike prior *in situ* XRD studies of hybrid perovskites,[8,27] we isolate the intrinsic behavior of inorganic $CsPbI_3$ by excluding humidity, oxygen, and permanent organic additives, enabling direct correlation of transformation rates with processing temperatures. Leveraging the Johnson-Mehl-Avrami-Kolmogorov (JMAK) model,[28–30] we fit the high-

View Article Online
DOI: 10.1039/D5TC01126D

temperature $CsPbI_3$ phase transformation kinetics and extracted the temperature-dependent transformation rate constants and the time until various δ-$CsPbI_3$ conversion fractions. Overall, these findings quantify the phase transition kinetics of $CsPbI_3$ thin films, which can inform processing protocols to access desired phases within experimental time/temperature constraints. $CsPbI_3$ is particularly prone to rapid phase conversion between 175°C and 250°C, as the time to initiate transformation to δ-$CsPbI_3$ is less than three minutes in this range. Since ensuring long-term phase stability is critical for practical photovoltaic applications, temperatures within this range may be particularly useful for accelerated stress testing.

Results

To quantify the phase transformation dynamics of $CsPbI_3$ thin films, ~500 nm β-$CsPbI_3$ films were prepared on Si substrates, as described in **Methods,** and as shown in **Fig. 1**. We then heated the films to 350°C to convert them into cubic α-$CsPbI_3$ and rapidly quenched them to temperatures between 150°C and 300°C to produce β/γ-$CsPbI_3$, before holding the films isothermally to monitor their phase transition to δ-$CsPbI_3$ under an optical microscope. Since β-$CsPbI_3$ and γ-$CsPbI_3$ have nearly identical optoelectronic properties, we cannot distinguish between these phases here. Thus, we refer to the temperature regimes measured by Marronnier et al. (β-$CsPbI_3$ between 281°C and 184°C, with γ-$CsPbI_3$ at lower temperatures) for their assignments.[31] As shown in the representative time series of micrographs in **Fig. 2a**, at 230°C, spherulites of δ-$CsPbI_3$ (bright red) grow radially at the expense of the black $CsPbI_3$ phase. After several minutes, the largest δ-$CsPbI_3$ spherulites have diameters on the order of millimeters. Tracking the radial growth of these spherulites, we plot their average interface velocity as a function of temperature in **Fig. 2b**. We find that interface velocity increases with temperature up to 250°C, where it peaks at 170 mm/min. Above this temperature, the spherulite interface velocities begin to slow as the thermodynamic driving force for phase transition decreases with increasing temperature.

To further characterize the extent and kinetics of structural transformations in $CsPbI_3$ thin films, we employed an *in situ* XRD setup with two heating stages, as described in **Methods**. As shown in **Fig.** 1, the absence of peak splitting and low symmetry reflections in the first XRD inset indicates that $CsPbI_3$ films convert to α-$CsPbI_3$ upon heating to 350°C. They were then rapidly transferred onto a heating stage inside the XRD sample chamber, pre-set to a temperature between 25°C and 300°C to convert them into metastable β- or γ-$CsPbI_3$. The samples were then held isothermally as XRD traces were collected to monitor the diminishing intensity of the (110) reflection of both β- and γ-$CsPbI_3$, located at 2θ=14.2°. A representative set of time-dependent XRD spectra is shown in **Fig. 3a** for a black $CsPbI_3$ film as it was

View Article Online
DOI: 10.1039/D5TC01126D

quenched from 350°C and held isothermally at 200°C. Integrating the area under the (110) reflection of β/γ-$CsPbI_3$ in each spectrum and normalizing by the integral of the first spectrum (which we assume represents 0% δ-$CsPbI_3$) yields the time-dependent fraction of the black $CsPbI_3$ phase in the film. Subtracting these quantities from unity yields the fraction of the film that has converted to δ-$CsPbI_3$, as plotted in **Fig. 3b**. To ensure the robustness and reproducibility of these measurements and to account for sample-to-sample variation, we repeated this same isothermal experiment several times with fresh samples at each temperature, as shown in **Fig. 3b,** where 6 films were characterized. Similar data collected at other temperatures are plotted in **Fig. S2**. Samples held at temperatures below 150°C converted too slowly for *in situ* XRD to be practical. Thus, the 100°C and 25°C samples were rested in a N_2 glovebox (on a hot plate in the case of 100°C) between ex-situ XRD measurements and photographed with the time stamps shown in **Fig. S3**. Structural transformation was measurable within 14 hours at 100°C, and after 41 days at 25°C. To probe the influence of the substrate in determining phase transformation kinetics, we also quenched $CsPbI_3$ films from 350°C to 200°C on glass substrates coated with indium tin oxide (ITO) and TiO_2 and quantified their phase transformation via XRD to compare with the transformation dynamics of $CsPbI_3$ on Si as shown in **Fig. S4**. The results show that transformation kinetics are virtually identical on both substrates.

To quantify the phase transition to δ-$CsPbI_3$, we fit the time-dependent fractional conversion data in **Fig. 3b** and **Fig. S2** using the JMAK equation:

$$f(t) = 1 - e^{-kt^n}, \tag{1}$$

where f represents the fraction of the film that has transformed to δ-$CsPbI_3$, *k* is the conversion rate constant, *t* is time, and *n* denotes the dimensionality and growth constant. The values of *k* and *n* are interdependent, and thus small changes to the dimensionality constant can compensate for large changes in the rate constant. To eliminate this interdependency, we note that the spherulite diameters are much larger than the film thickness and nucleation appears to be heterogeneous and instantaneous, as evidenced by similar spherulite radii in **Fig. 2a**. We therefore fixed the value of the Avrami exponent to n = 2, corresponding to 2-dimensional growth.[32] A representative fit to the 200°C transformation kinetics using the JMAK equation with *n* = 2 is shown in **Fig. 3b** with 95% confidence interval bounds. The JMAK equation fits the $CsPbI_3$ phase transformation data collected between 150°C and 300°C well. The parameters extracted from these fits are reported in **Table 1**, where transformation rate constants vary from 3.4×10^{-10} s^{-2} at 300°C to 6.6×10^{-7} s^{-2} at 225°C.

View Article Online
DOI: 10.1039/D5TC01126D

The time- and temperature-dependent XRD data allow us to generate the time-temperature-transformation (TTT) diagram for $CsPbI_3$ films shown in **Fig. 4**. We denote the δ-to-α-$CsPbI_3$ transformation temperature with a horizontal line at 326°C based on differential scanning calorimetry data shown in **Fig. S5**. This is similar to the 320°C transition temperature reported by Ke et al.[33] We also added horizontal lines at 281°C and 184°C corresponding to the α- to β-$CsPbI_3$ and the β- to γ-$CsPbI_3$ transitions reported by Marrionier et al.[31] The fastest transformation to δ-$CsPbI_3$ occurred at 225°C where 1% of the film converted after just under 120 seconds, and 50% of the film converted in 17 minutes. The transformation rate decreased with temperature from 225°C, with the transformation at 25°C requiring over a month in N_2 to accumulate an appreciable amount of δ-$CsPbI_3$, as shown in the photographs in **Fig. S3**.

Discussion

Previously, Marronnier et al. measured the phase transition temperatures between the four $CsPbI_3$ polymorphs by gradually cooling a powder sample under vacuum at 2.5°C/min.[31] Here, we attempted to more closely replicate the thin-film form factor of practical $CsPbI_3$ photoactive layers and their fabrication conditions by rapidly quenching thin films from the α-phase.[23] The isothermal nature of our experiments also keeps the energetics (i.e., thermodynamic driving force and probability of hopping over the kinetic barrier) constant over the course of the measurement. We performed our experiments in N_2 to emulate an encapsulated solar cell, as humidity is known to have a significant catalytic effect on $CsPbI_3$ phase transitions.[34] For example, in a study of the atmospheric phase stability of $CsPbI_3$, Straus et al. demonstrated that γ-$CsPbI_3$ is kinetically stable in vacuum (>39 days) and dry oxygen (>25 min) but rapidly transforms to δ-$CsPbI_3$ under humid argon flow (<1 min).[34] The absence of δ-$CsPbI_3$ conversion in vacuum after 39 days is comparable to our finding that a γ-$CsPbI_3$ film began to convert to δ-$CsPbI_3$ after 41 days in an inert atmosphere.

The overall phase transformation rate is influenced by several factors, including the transformation driving force and kinetic limitations, which both depend strongly on temperature. The chemical potential difference between the initial and final phases increases with undercooling and causes the transformation rate to increase as the $CsPbI_3$ film cools below the δ- to α-$CsPbI_3$ transition temperature. Conversely, as temperature decreases, reduced thermal energy decreases atomic mobility, which causes the transformation to slow. Competition between the driving force and kinetic limits thus governs the phase transformation rate as a function of temperature. As a result of this competition, a peak spherulite boundary velocity is observed in **Fig. 2b** at 250°C. The tradeoff between kinetic limitations and transformation driving force is often observed in polymorphic materials that undergo solid-solid

View Article Online
DOI: 10.1039/D5TC01126D

phase transformations, such as carbon-containing steels.[35] For example, in eutectic steel, austenite transforms slowly into pearlite at temperatures close to the transition temperature (700°C), slowly into bainite at temperatures (~300°C) far from the transition temperature, and quickly transforms into bainite at 550°C. Additionally, we note that previous studies suggest that the internal energy of high-symmetry $CsPbI_3$ phases is not minimized in a monomorphous state.[36,37] Rather, these phases contain networks of local symmetry-breaking distortions such as Jahn-Teller distortions,[38] octahedral tilting,[36] and small shifts in atomic equilibrium positions from the expected Wyckoff positions.[14,37–39] Because they are local, these patterns are generally not measurable with structural characterization techniques such as XRD.

Another potential source of variance in kinetics is the substrate beneath the $CsPbI_3$ layer. Here, we primarily employed bare Si due to its atomically smooth surface, chemical inertness, lack of ions and Lewis base/acid sites, and thin amorphous oxide layer, which we thus expect to interact minimally with $CsPbI_3$. However, we also measured the time-dependent fractional conversion of $CsPbI_3$ films on glass coated with ITO and TiO_2 for comparison to Si after quenching from 350°C to 200°C, as shown in **Fig. S4**. The $CsPbI_3$ films deposited on this device-relevant electrode/electron-transport layer exhibited time-dependent fractional conversions that aligned closely with those measured on Si substrates over $6x10^3$ s. This suggests that, under these conditions, transformation kinetics are relatively insensitive to substrate roughness, interfacial strain, and chemical interactions. One effect we do observe is that the thermal mass, thickness, and thermal conductivity of the substrate do play a role in how quickly the film heats and converts (e.g., 2.2 mm-thick glass substrates coated with fluorinated tin oxide convert to α-$CsPbI_3$ more slowly upon heating). In this work, we tried to maximize thermal responsiveness and minimize time before reaching the isothermal setpoints by using thin (<0.7 mm) substrates for all measurements.

The overall transformation rate is the product of the δ-$CsPbI_3$ boundary velocity and nucleation rate (which also results from competition between the driving force and atomic mobility).[35] The temperature-dependence of nucleation causes the overall transformation rate to peak at a slightly lower temperature (225°C in **Fig. 4**) than the peak boundary velocity (250°C in **Fig. 2b**). This peak transformation rate is also reflected in the JMAK fits in **Table 1**, where a rate of $6.6x10^{-7}$ s^{-2} is found at 225°C. The data represented visually in the TTT can be used to develop processing routes for $CsPbI_3$ as well as thermally accelerated phase stability testing protocols. Films will begin to transition to δ-$CsPbI_3$ within ~2 minutes at 225°C, while much longer processing windows are available at both higher and lower temperatures. Similarly, 225°C is a good temperature to test the efficacy of phase-stabilization schemes under maximum

View Article Online
DOI: 10.1039/D5TC01126D

stress. Understanding the kinetic limit-driving force tradeoff is essential for optimizing processing parameters and designing $CsPbI_3$-based devices with enhanced stability and performance.

Conclusions

In this study, we employed a combination of *in situ* XRD and optical microscopy to study the transformation kinetics of photoactive $CsPbI_3$ phases into δ-$CsPbI_3$ in N_2 at temperatures ranging from 150°C to 300°C after quenching thin films from 350°C. We also studied the transformation kinetics of $CsPbI_3$ films at 100°C and room temperature using *t al* XRD and optical photography. The results of these experiments were used as a basis to create a $CsPbI_3$ TTT diagram. The peak transition rate occurs at 225°C, where δ-$CsPbI_3$ is detected within 120 seconds of quenching from 350°C, while films aged at room temperature require nearly six weeks to begin transforming. The onset of δ-$CsPbI_3$ formation in thin films initiates via heterogeneous nucleation and grows into spherulitic domains with boundaries that expand at a constant temperature-dependent velocity. The transformation kinetics fit well with the JMAK model, assuming 2-dimensional growth. The results of this study can be used to inform processing routes for photoactive $CsPbI_3$ films and to identify the highest stress conditions for accelerated phase stability testing of devices comprising $CsPbI_3$ active layers with various phase-stabilization schemes.

Acknowledgments

The authors thank First Solar, Inc. for fruitful discussions and for supporting this work. All authors acknowledge support from the U.S. Department of Energy's Office of Energy Efficiency and Renewable Energy (EERE) under Solar Energy Technologies Office (SETO) Agreement Number DE-EE0010503. The authors acknowledge the use of Princeton's Imaging and Analysis Center, which is partially supported through the Princeton Center for Complex Materials (PCCM), a National Science Foundation (NSF)-MRSEC program (DMR-2011750). R.H. thanks the National Science Foundation Graduate Research Fellowship Program under Grant No. DGE-2039656 for supporting this work.

View Article Online
DOI: 10.1039/D5TC01126D

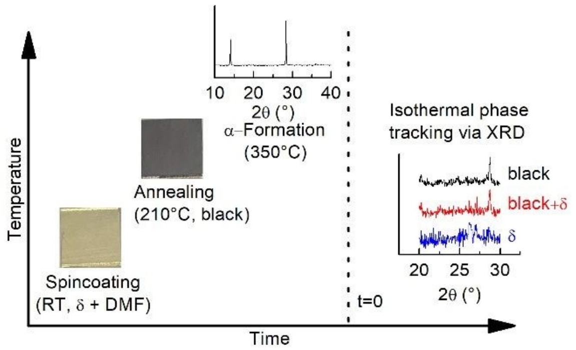

Figure 1 | Diagram showing the temperature and sequence of the processes used to prepare $CsPbI_3$ thin films for time-dependent isothermal polymorph identification measurements conducted between 150°C and 300°C. The image in the lower-left corner of the plot is a photograph of a $CsPbI_3$ film immediately after spin-coating. To the right of that is an image of a β-$CsPbI_3$ film immediately after annealing at 210°C for 5 min. At the top of the figure is an *in situ* XRD plot of α-$CsPbI_3$ at 350°C. The rightmost plot shows $CsPbI_3$ XRD spectra evolving from β-$CsPbI_3$ to δ-$CsPbI_3$ after the film was quenched from 350°C and held isothermally (at 225°C in this case) for XRD characterization.

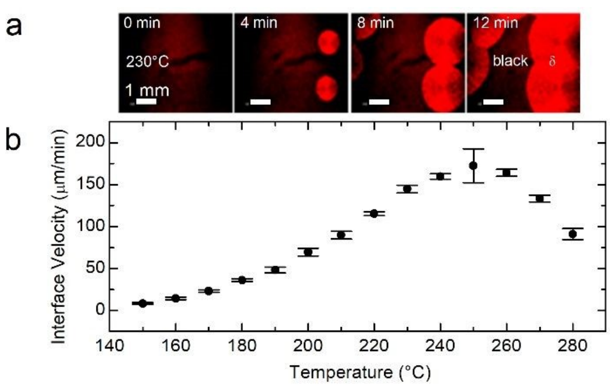

Figure 2 | a) Optical microscope images showing the phase conversion of a black $CsPbI_3$ film to δ-$CsPbI_3$ while held isothermally at 230°C. A 1mm scale bar is included on each panel. **b)** The temperature dependence of the perovskite (β, or γ)-$CsPbI_3$ to δ-$CsPbI_3$ interface velocity derived from time-dependent optical micrographs. Horizontal bars represent the minimum and maximum velocities recorded. At least 3 samples were characterized at each temperature.

View Article Online
DOI: 10.1039/D5TC01126D

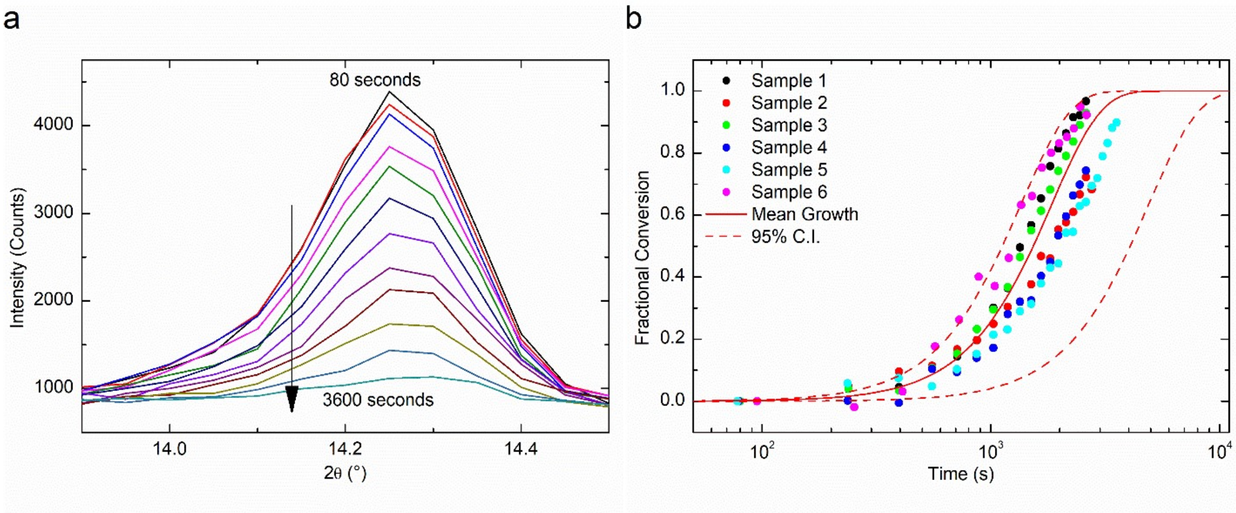

Figure 3 | a) XRD traces showing the time evolution of the (110) reflection of a β/γ-$CsPbI_3$ film quenched from 350°C and held isothermally at 200°C during measurement. b) The fraction converted to δ-$CsPbI_3$ tracked for 6 different perovskite films having undergone quenching from 350°C and isothermal transformation at 200°C. The fractional conversion was calculated by integrating the area under the (110) reflection and assuming 0% conversion at the first measurement point. The fractional conversion vs. time curves for each sample were fitted with the JMAK equation by varying the JMAK rate constant and holding the dimensionality constant at two. The solid and dashed lines represent JMAK projections using the mean rate constant and its 95% confidence intervals, respectively.

View Article Online
DOI: 10.1039/D5TC01126D

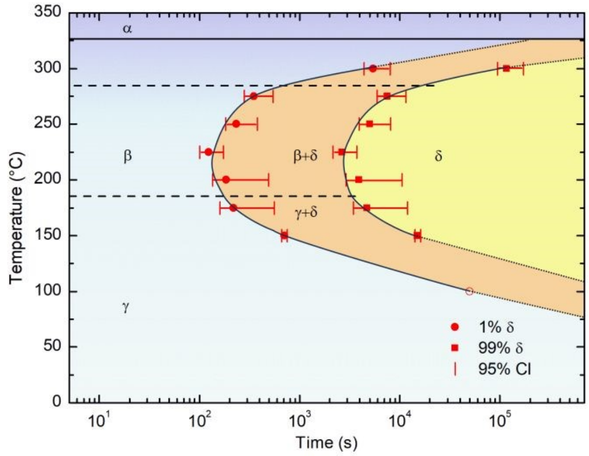

Figure 4 | A time-temperature-transformation diagram for $CsPbI_3$ thin films. Dashed lines at 281°C and 184°C denote temperature limits of β and γ stability, respectively, as reported by Marronier et al.[31] The solid line at 326°C marks the δ-α transformation temperature determined by DSC (**Fig. S5**). Error bars signify the 95% confidence interval, and the extrapolated dotted lines represent linear projections of polymorphic stability limits. The hollow circle at 100°C signifies a photographed film's approximate onset of δ-$CsPbI_3$ on a hot plate (**Fig. S3**).

Table 1| Avrami rate constants, 1%, 50%, and 99% conversion times for $CsPbI_3$ transformations from perovskite phases to the δ-phase. The upper and lower bounds of the 95% confidence interval for each parameter are given in brackets.

T (°C)	k	$\times 10^{-7}$ (s^{-2})	t_1	$\times 10^2$ (s)	t_{50}	$\times 10^2$ (s)	t_{99}	$\times 10^2$ (s)
150	0.20	[0.18, 0.23]	7.0	[6.6, 7.5]	59	[55,62]	150	[140, 160]
175	2.1	[0.32, 3.9]	2.2	[1.6, 5.6]	18	[13,47]	47	[34, 12]
200	3.0	[0.42, 5.5]	1.8	[1.4, 4.9]	15	[11,41]	39	[29, 10]
225	6.6	[3.3, 9.9]	1.2	[1.0, 1.7]	10	[8.4,14]	26	[22, 37]
250	1.8	[0.70, 3.0]	2.3	[1.8, 3.8]	20	[15,31]	50	[39, 81]
275	0.81	[0.34, 1.3]	3.5	[2.8, 5.4]	29	[23,45]	75	[60, 120]
300	0.0034	[0.0016, 0.0052]	55	[44, 80.]	450	[370,660]	1200	[940, 1700]

View Article Online
DOI: 10.1039/D5TC01126D

References

1 Y. Liu, Z. Yang, D. Cui, X. Ren, J. Sun, X. Liu, J. Zhang, Q. Wei, H. Fan, F. Yu, X. Zhang, C. Zhao and S. Liu, *Adv. Mater.*, 2015, **27**, 5176–5183.
2 A. Suhail, A. Saini, S. Beniwal and M. Bag, *J. Phys. Chem. C*, 2023, **127**, 17298–17306.
3 H. J. Feng, T. R. Paudel, E. Y. Tsymbal and X. C. Zeng, *J. Am. Chem. Soc.*, 2015, **137**, 8227–8236.
4 S. Liu, V. P. Biju, Y. Qi, W. Chen and Z. Liu, *NPG Asia Mater.*, 2023, **15**, 27.
5 Z. Hu, C. Ran, H. Zhang, L. Chao, Y. Chen and W. Huang, *Engineering*, 2023, **21**, 15–19.
6 M. H. Futscher and B. Ehrler, *ACS Energy Lett.*, 2016, **1**, 863–868.
7 T. Leijtens, K. A. Bush, R. Prasanna and M. D. McGehee, *Nat. Energy*, 2018, **3**, 828–838.
8 A. Luongo, B. Brunetti, S. Vecchio Ciprioti, A. Ciccioli and A. Latini, *J. Phys. Chem. C*, 2021, **125**, 21851–21861.
9 G. Abdelmageed, C. Mackeen, K. Hellier, L. Jewell, L. Seymour, M. Tingwald, F. Bridges, J. Z. Zhang and S. Carter, *Sol. EEnergy Mater. Sol. Cells*, 2018, **174**, 566–571.
10 R. J. Sutton, G. E. Eperon, L. Miranda, E. S. Parrott, B. A. Kamino, J. B. Patel, M. T. Hörantner, M. B. Johnston, A. A. Haghighirad, D. T. Moore and H. J. Snaith, *Adv. Energy Mater.*, 2016, **6**, 1502458.
11 P. Becker, J. A. Márquez, J. Just, A. Al-Ashouri, C. Hages, H. Hempel, M. Jošt, S. Albrecht, R. Frahm and T. Unold, *Adv. Energy Mater.*, 2019, **9**, 1900555.
12 J. Satta, A. Casu, D. Chiriu, C. M. Carbonaro, L. Stagi and P. C. Ricci, *Nanomaterials*, 2021, **11**, 1823.
13 P. Chhillar, B. P. Dhamaniya, S. K. Pathak and S. Karak, *ACS Appl. Electron. Mater.*, 2022, **4**, 5368–5378.
14 D. B. Straus, S. Guo, A. M. Abeykoon and R. J. Cava, *Adv. Mater.*, 2020, **32**, 2001069.
15 Y. Wang, X. Liu, T. Zhang, X. Wang, M. Kan, J. Shi and Y. Zhao, *Angew. Chem.*, 2019, **131**, 16844–16849.
16 Y. Hu, F. Bai, X. Liu, Q. Ji, X. Miao, T. Qiu and S. Zhang, *ACS Energy Lett.*, 2017, **2**, 2219–2227.
17 P. Luo, W. Xia, S. Zhou, L. Sun, J. Cheng, C. Xu and Y. Lu, *J. Phys. Chem. Lett.*, 2016, **7**, 3603–3608.
18 Y. Wang, T. Zhang, M. Kan and Y. Zhao, *J. Am. Chem. Soc.*, 2018, **140**, 12345–12348.
19 B. Zhao, S.-F. Jin, S. Huang, N. Liu, J.-Y. Ma, D.-J. Xue, Q. Han, J. Ding, Q.-Q. Ge, Y. Feng and J.-S. Hu, *J. Am. Chem. Soc.*, 2018, **140**, 11716–11725.
20 X. Zhao, T. Liu, Q. C. Burlingame, T. Liu, R. Holleyiii, G. Cheng, N. Yao, F. Gao and Y.-L. Loo, *Science*, 2022, **377**, 307–310.
21 J. Wang, Y. Che, Y. Duan, Z. Liu, S. Yang, D. Xu, Z. Fang, X. Lei, Y. Li and S. (Frank) Liu, *Adv. Mater.*, 2023, **35**, 2210223.
22 J. Yuan, D. Zhang, B. Deng, J. Du, W. C. H. Choy and J. Tian, *Adv. Funct. Mater.*, 2022, **32**, 2209070.
23 J. A. Steele, H. Jin, I. Dovgaliuk, R. F. Berger, T. Braeckevelt, H. Yuan, C. Martin, E. Solano, K. Lejaeghere, S. M. J. Rogge, C. Notebaert, W. Vandezande, K. P. F. Janssen, B. Goderis, E. Debroye, Y.-K. Wang, Y. Dong, D. Ma, M. Saidaminov, H. Tan, Z. Lu, V. Dyadkin, D. Chernyshov, V. Van Speybroeck, E. H. Sargent, J. Hofkens and M. B. J. Roeffaers, *Science*, 2019, **365**, 679–684.
24 G. E. Eperon, G. M. Paternò, P. Paternò, R. J. Sutton, A. Zampetti, B. Amir, A. Haghighirad, F. Cacialli and H. J. Snaith, *J. Mater. Chem. A*, 2015, **3**, 19688–19695.
25 T. Liu, X. Zhao, X. Zhong, Q. C. Burlingame, A. Kahn and Y. L. Loo, *ACS Energy Lett.*, 2022, **7**, 3531–3538.
26 R. Bystricky, S. K. Tiwari, P. Hutar and M. Sykora, *Inorg. Chem.*, **64**, 12826–12838.
27 E. J. Juarez-Perez, Z. Hawash, S. R. Raga, L. K. Ono and Y. Qi, *Energy Environ. Sci.*, 2016, **9**, 3406–3410.
28 M. Avrami, *J. Chem. Phys*, 1939, **7**, 1103–1112.
29 M. Avrami, *J. Chem. Phys*, 1940, **8**, 212–224.
30 M. Avrami, *J. Chem. Phys*, 1941, **9**, 177–184.

View Article Online
DOI: 10.1039/D5TC01126D

31 A. Marronnier, G. Roma, S. Boyer-Richard, L. Pedesseau, J. M. Jancu, Y. Bonnassieux, C. Katan, C. C. Stoumpos, M. G. Kanatzidis and J. Even, *ACS Nano*, 2018, **12**, 3477–3486.
32 C. Berlic and V. Barna, *Digest J. Nanomater.*, 2016, **11**, 159–165.
33 F. Ke, C. Wang, C. Jia, N. R. Wolf, J. Yan, S. Niu, T. P. Devereaux, H. I. Karunadasa, W. L. Mao and Y. Lin, *Nat Commun*, 2021, **12**, 1–8.
34 D. B. Straus, S. Guo and R. J. Cava, *J. Am. Chem. Soc.*, 2019, **141**, 11435–11439.
35 M. F. Ashby and D. R. H. Jones, *Engineering Materials 2 - An Introduction to Microstructures and Processing*, Butterworth-Heinemann, 4th edn., 2013.
36 X.-G. Zhao, G. M. Dalpian, Z. Wang and A. Zunger, *Phys. Rev. B*, 2020, **101**, 155137.
37 L. Octavio De Araujo, C. R. C. Rêgo, W. Wenzel, F. P. Sabino and D. Guedes-Sobrinho, *J. Phys. Chem. C*, 2022, **126**, 2131–2140.
38 X.-G. Zhao, Z. Wang, O. Malyi and A. Zunger, *Mater. Today*, 2021, **49**, 107–122.
39 A. N. Beecher, O. E. Semonin, J. M. Skelton, J. M. Frost, M. W. Terban, H. Zhai, A. Alatas, J. S. Owen, A. Walsh and S. J. L. Billinge, *ACS Energy Lett.*, 2016, **1**, 880–887.

View Article Online
DOI: 10.1039/D5TC01126D

The data supporting this work are included in the manuscript and supporting information. Additional raw files are available from the corresponding authors upon reasonable request, and can be made available in an online repository prior to publication if required by *Journal of Materials Chemistry C*.